Chemical Science

ROYAL SOCIETY OF CHEMISTRY

EDGE ARTICLE

View Article Online
View Journal | View Issue

Cite this: *Chem. Sci.*, 2023, **14**, 7743

All publication charges for this article have been paid for by the Royal Society of Chemistry

Received 9th May 2023
Accepted 19th June 2023

DOI: 10.1039/d3sc02338a

rsc.li/chemical-science

Revealing the role of nitroxyl during hepatic ischemia-reperfusion injury with a NIR-II luminescent nanoprobe†

Chenchen Li,‡ Wenqiang Bi,‡ Tao Liang, Zhen Li * and Zhihong Liu *

Hepatic ischemia-reperfusion injury (HIRI) can severely impair liver function and has a potential relationship with reactive nitrogen species. Nitroxyl (HNO) has been discovered to be involved in some biological functions and pharmacological activities. However, till now, there has been no knowledge of the role of HNO in the HIRI process, mainly because accurately tracking its fluctuation at the molecular level *in vivo* is extremely difficult. Herein, we developed a responsive ratiometric near-infrared-II (NIR-II) nanoprobe with rare earth ions-doped nanoparticles (RENPs) as the luminophore and a molecular trigger that can specifically react with HNO to regulate the NIR-II emission of RENPs. With this nanoprobe, we revealed the relationship between HNO and the HIRI process and demonstrated that HNO may be a product of stress reactions during HIRI. This work not only creates a useful tool for visually tracking HNO *in vivo* but also provides first-hand information about its role in HIRI.

Introduction

Hepatic ischemia-reperfusion injury (HIRI) results from prolonged liver ischemia under conditions of inadequate oxygen and nutrient supply and subsequent restoration of blood perfusion, which is an inevitable complication during various liver surgery procedures, including liver transplantation, resection, and so forth. HIRI has become one of the key factors affecting the success rate of liver surgery and postoperative survival of patients.[1,2] HIRI can be alleviated or cured if timely therapeutic interventions are conducted, which requires rapid and accurate evaluation of the HIRI process.[3] Traditional clinical diagnostic methods of liver injury mainly include serum analysis of biomarkers, such as alanine aminotransferase (ALT) and aspartate aminotransferase (AST), liver biopsy, and imaging techniques. However, serum analysis cannot reflect the changes in the concentration of specific targets that vary significantly *in situ* but not in serum, which is generally used for the diagnosis of liver injury, instead of molecular-level pathology. Liver biopsy can induce secondary injury, and it presents poor evaluation accuracy resulting from the different observers and sampling errors.[4] Imaging techniques, such as magnetic resonance imaging (MRI), ultrasound, and computed tomography (CT), suffer from slow detection rates, poor accuracy, or low sensitivity.[5] Hence, the development of *in situ* detection approaches for observation of HIRI at the molecular level with high speed, sensitivity, and specificity, along with minimal invasiveness, are urgently needed to understand the pathology of HIRI.

HIRI is accompanied by oxidative stress that leads to the abnormal production of reactive oxygen species (ROS) and reactive nitrogen species (RNS),[6] and detection of these species may provide information on the occurrence and progression of HIRI at the molecular level. Among the commonly known ROS and RNS, nitroxyl (HNO) is quite enigmatic and suggested to possess important biological and pharmacological functions, as revealed by some biochemical research methods.[7] However, there is no knowledge on the role of HNO during the HIRI process so far because its detection with high sensitivity and specificity in deep-seated organs, such as the liver, in the living body is extremely difficult. Near-infrared-II (NIR-II) fluorescence imaging is a recognized tool for detecting biomolecules in living systems, owing to its excellent selectivity, high spatial resolution, and adequate penetration depth in biological tissues.[8–13] However, presently there is no NIR-II fluorescent probe for HNO available. This is fundamentally restricted by the working principle of reaction-based fluorescent probes. Specifically, the recognition moiety that selectively responds to HNO, which is based on the Staudinger reaction between 2-(diphenylphosphino)benzoate and HNO,[14,15] is unable to modulate the emission of all current NIR-II fluorophores *via* any known mechanism.

To circumvent the above dilemma, we decided to turn to alternative luminophores and seek new strategies for probe construction. Rare earth ions-doped nanoparticles (RENPs) are

College of Health Science and Engineering, College of Chemistry and Chemical Engineering, Hubei University, Wuhan 430062, China. E-mail: zhenli@hubu.edu.cn; zhhliu@whu.edu.cn

† Electronic supplementary information (ESI) available. See DOI: https://doi.org/10.1039/d3sc02338a

‡ These authors contributed equally to this work.

a kind of potential optical materials for NIR-II imaging due to their multichannel excitation and emission, good biocompatibility, and high chemical and photostability.[16–20] Herein, we fabricated an HNO-responsive NIR-II fluorescent probe using RENPs as the luminophore and a molecular trigger that specifically reacts with HNO to modulate the NIR-II emission of RENPs upon the reaction. The as-prepared nanoprobe, named as Cy-TP-RENPs, mainly includes three components (Scheme 1A): RENPs comprising $NaYF_4$:Yb,Er,Ce@$NaYF_4$:Nd, a NIR dye (Cy-TP), and an amphiphilic molecule (DSPE-PEG_{2000}), where the RENPs with dual excitation bands (808 and 980 nm) act as a signal reporter with down-conversion luminescence (DCL) around 1550 nm; Cy-TP, with emission around 810 nm, serves as the modulator of RENPs, as well as a recognition unit for HNO, and DSPE-PEG_{2000} endows the probe with water dispersibility. Due to the spectral overlap between the absorption spectrum of Nd^{3+} and the emission spectrum of Cy-TP, the excited-state energy of Cy-TP can be effectively transferred to Nd^{3+} upon excitation with 808 nm laser through a non-radiative energy transfer process, yielding enhanced NIR-II luminescence of RENPs. Cy-TP transforms to Cy-HNO after HNO reacts with the 2-(diphenylphosphino)-benzoate through the Staudinger reaction to yield the corresponding aza-ylide; this is followed by a rearrangement reaction (Fig. S1†) that leads to a change in the conjugated system of the molecule and decreased radiative relaxation around 810 nm, suppressing the energy transfer to Nd^{3+} and weakening the NIR-II luminescence of RENPs under 808 nm excitation. Meanwhile, the luminescence signal of RENPs at 1550 nm under excitation with a 980 nm laser, which originates from the excitation of doped Yb^{3+} and leads to subsequent energy transfer to Er^{3+}, remains stable and acts as the internal calibration signal for constructing a ratiometric NIR-II luminescent probe. As known, ratiometric readout guarantees the accuracy and reliability of the imaging results as it can avoid possible uncertainties, resulting from uneven distribution of the probe in the living body, variation in the biological environment, instrumental parameters, *etc.* With this probe, we successfully observed the fluctuation in HNO levels during the HIRI process and also disclosed its protective effect on hepatocytes (Scheme 1B).

Results and discussion

Photophysical properties of Cy-TP

Cy-TP was synthesized with heptamethine cyanine as the scaffold and 2-(diphenylphosphino)benzoate as the recognizing motif for HNO. The heptamethine cyanine scaffold was selected in consideration of its spectral match with Nd^{3+}, which allows enhancement of the luminescence of Nd^{3+}-doped RENPs.[21] To facilitate the assembly of Cy-TP and RENPs, two long hydrophobic alkyl chains were introduced into Cy-TP to increase its hydrophobicity; these chains can be encapsulated into the hydrophobic cavity formed between DSPE-PEG_{2000} and RENPs. The energy levels of the highest occupied molecular orbital (HOMO) and lowest-unoccupied molecular orbital (LUMO) electrons were calculated according to the density functional theory (DFT), displaying that the energy gap of HOMO–LUMO in Cy-TP was 2.06 eV (Fig. S2†). Cy-TP displayed a strong absorption peak at 780 nm with a molar absorption coefficient of 6.16 $\times$ 10^4 L mol^{-1} cm^{-1} (Fig. S3A and B†). Its molar absorption coefficient at 808 nm (the wavelength of the commercial laser as excitation source) in the hydrophobic layer was 4.16 $\times$ 10^4 L

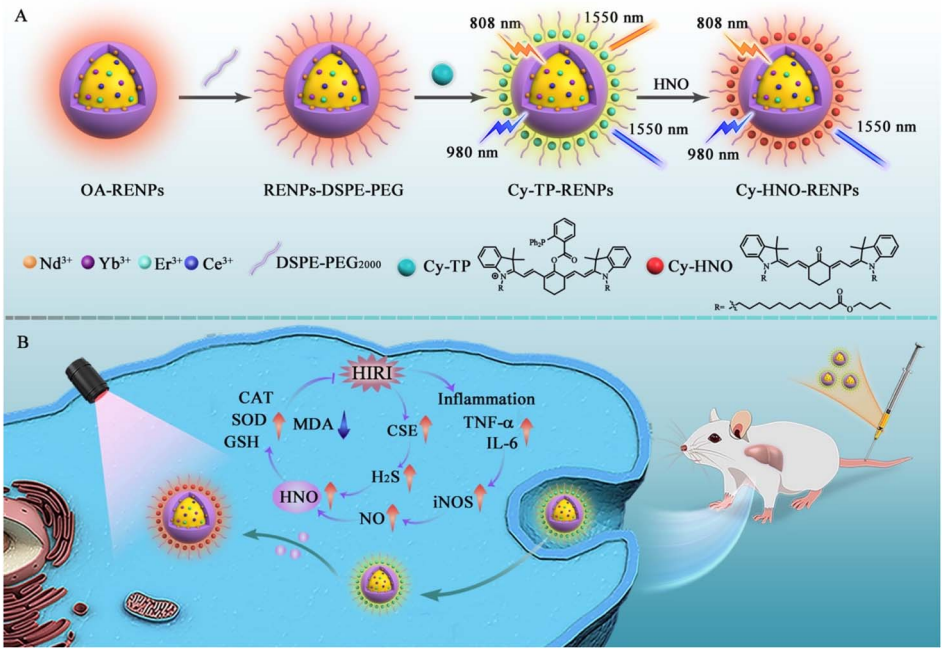

Scheme 1 Schematic illustration of the construction of HNO-responsive ratiometric NIR-II luminescent nanoprobe, Cy-TP-RENPs (A) and its use in the living body (B).

mol^{-1} cm^{-1} (Fig. S3C†) and was ~5.4 × 10^4 times higher than that of Nd^{3+} (0.77 L mol^{-1} cm^{-1}), implying that the direct absorption by Nd^{3+} at 808 nm was insignificant and that Cy-TP was the dominant light harvester. Besides, Cy-TP emitted a bright fluorescence signal at ~810 nm that matched well with the absorption of Nd^{3+} (Fig. 1A), making it a suitable modulator to enhance the luminescence of RENPs. After reacting with HNO, both the absorption centered at 780 nm and emission at 810 nm of Cy-TP was reduced significantly (Fig. 1B and C), meaning that the ability of the reaction product, *i.e.*, Cy-HNO, to improve the NIR-II luminescence of RENPs would be weakened. Meanwhile, a new absorption peak at ~550 nm and a fluorescence peak at ~620 nm appeared, which increased in a [HNO]-dependent manner (Fig. S4†), showing that Cy-TP was converted to Cy-HNO.

Fabrication of Cy-TP-RENPs

RENPs with the composition of $NaYF_4$:20%Yb,2%Er,5% Ce@$NaYF_4$:20%Nd were synthesized by a seed-mediated epitaxial growth method.[22] Such an elemental composition was designed to offer two energy-transfer chains within the probe (Fig. 2A): (1) the antenna sensitization cascade Cy-TP → Nd^{3+} → Yb^{3+} → Er^{3+} under 808 nm excitation, which depends on the target and functions as the detection signal; (2) the direct excitation cascade Yb^{3+} → Er^{3+} under 980 nm excitation, which is independent of the target and serves as the calibration signal. Ce^{3+} doped in the core was able to promote the nonradiative $^4I_{11/2}$ → $^4I_{13/2}$ relaxation of Er^{3+}, facilitating the NIR-II emission of RENPs around 1550 nm ($^4I_{13/2}$ → $^4I_{15/2}$). As shown in Fig. 2B and C, the prepared RENPs were uniform spherical nanoparticles with a core diameter of 39.2 ± 2.2 nm and a shell thickness of 1 nm (Fig. S5†). The composition of RENPs was also confirmed by the annular dark field-scanning image (ADF) and corresponding elemental mapping (Fig. 2D). X-ray diffraction (XRD) illustrated that RENPs featured highly crystalline hexagonal phases (Fig. S6†). To construct Cy-TP-RENPs, oleic acid-coated RENPs (OA-RENPs) were first assembled with the amphiphilic polymer, DSPE-PEG_{2000}, through a hydrophobic interaction to form a hydrophobic cavity, in which Cy-TP could be encapsulated. As presented in the Fourier transform infrared (FTIR) spectrum of Cy-TP-RENPs, the characteristic peaks at 1730 and 1633 cm^{-1} could be assigned to C=O stretching of the ester group of Cy-TP and the amide group in DSPE-PEG_{2000}, respectively (Fig. S7A†). The UV-vis absorption spectrum of Cy-TP-RENPs exhibited the characteristic peak of Cy-TP at ~780 nm (Fig. S7B†). In addition, because of the encapsulation of positively charged Cy-TP in the hydrophobic cavity, the zeta potential of RENPs shifted from −14 mV to −1 mV, and the hydrodynamic diameter increased from 43 nm to 105 nm (Fig. S8†). All these characterizations demonstrated that the nanoprobes, Cy-TP-RENPs, were successfully constructed. Furthermore, TEM images of Cy-TP-RENPs displayed that their size and morphology were close to RENPs, suggesting that the surface modification process had no obvious effect on the morphology of RENPs (Fig. S9†).

Ratiometric response of Cy-TP-RENPs to HNO

We investigated the performance of Cy-TP-RENPs towards HNO in buffer solutions. As shown in Fig. S10,† after incubation with Angeli's salt (AS, a commonly used HNO donor compound), there was no significant change in the luminescence intensity of RENPs at 1550 nm upon excitation with 980 or 808 nm laser, indicating that the presence of HNO does not affect the intrinsic luminescence of RENPs. We then optimized the loading capacity of Cy-TP on the surface of RENPs. As shown in Fig. 3A and B, NIR-II luminescence intensity at 1550 nm under 808 nm laser excitation ($I_{Ex\ 808\ nm}$) gradually enhanced with the increase in Cy-TP loading capacity, and reached the maximum with the loading capacity of 29.3 nmol mg^{-1} RENPs, which was calculated according to the absorbance of Cy-TP-RENPs at 780 nm and its molar absorption coefficient. It is noteworthy that the NIR-II luminescence intensity dropped as the loading capacity continued to increase. This phenomenon could have resulted from the aggregation-caused quenching effect of Cy-TP with higher concentrations on the surface of RENPs. In the meantime, the NIR-II luminescence under 980 nm laser excitation ($I_{Ex\ 980\ nm}$) remained stable to serve as a reference signal (Fig. 3C). Subsequently, we verified the HNO detection ability of Cy-TP-RENPs with the optimal loading capacity of Cy-TP in buffer solution. After incubating a certain concentration of AS with Cy-TP-RENPs in solution, the ratiometric signal of $I_{Ex\ 980\ nm}/I_{Ex\ 808\ nm}$ immediately increased and reached a platform within

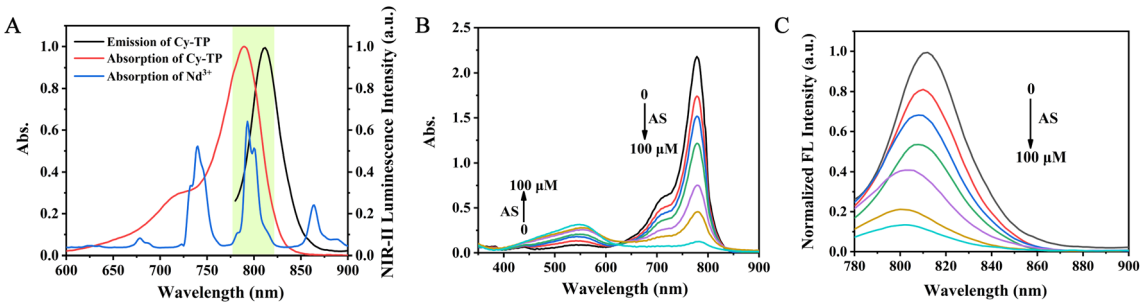

Fig. 1 (A) Spectral overlap between the emission of Cy-TP and the absorption of Nd^{3+}. The absorption spectrum of Nd^{3+} was obtained from $NdCl_3$ (a.q.). (B) Absorption spectra and (C) emission spectra of Cy-TP under 770 nm excitation after responding to different concentrations of HNO.

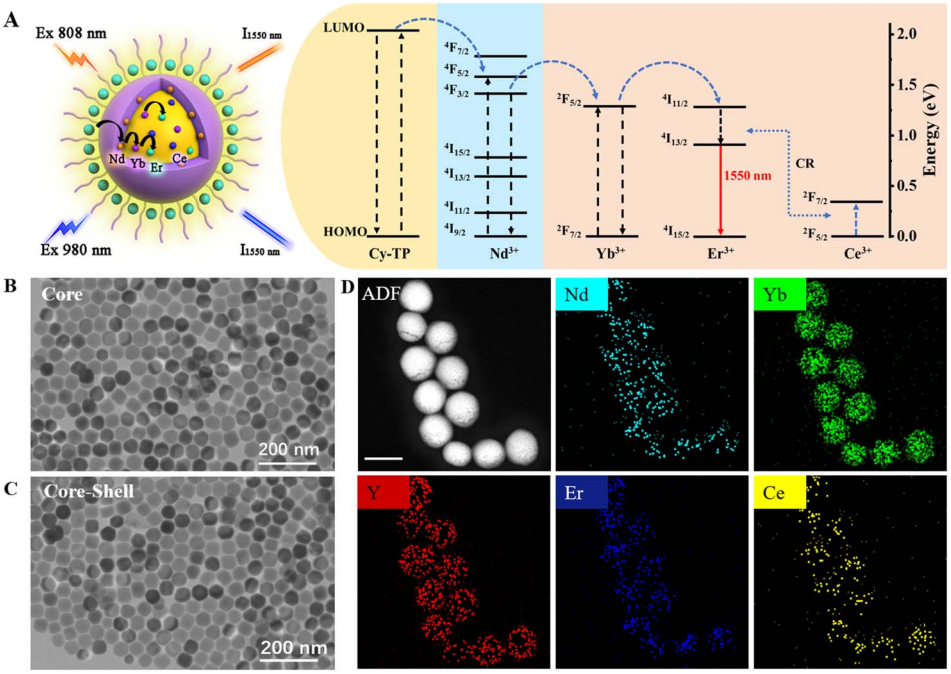

Fig. 2 (A) Schematic illustration of the RENPs structure ($NaYF_4$:20%Yb,2%Er,5%Ce@$NaYF_4$:20%Nd) and the energy transfer process. TEM images of core ($NaYF_4$:20%Yb,2%Er,5%Ce) (B) and core–shell structured RENPs ($NaYF_4$:20%Yb,2%Er,5%Ce@$NaYF_4$:20%Nd) (C). (D) ADF-STEM image and corresponding elemental mapping (Nd, Yb, Y, Er, and Ce) of the obtained RENPs (scale bar: 100 nm).

30 min, indicating that this nanoprobe possessed a high response speed (Fig. S11†). Thus, Cy-TP-RENPs were incubated with AS for 30 min to ensure a complete reaction in the subsequent experiments. As shown in Fig. 3D, under the excitation of an 808 nm laser, $I_{Ex\ 808\ nm}$ of Cy-TP-RENPs was attenuated in a stepwise manner with an increase in the concentration of HNO. Meanwhile, $I_{Ex\ 980\ nm}$ of Cy-TP-RENPs remained unchanged (Fig. 3E). The ratiometric signal of I_{Ex}

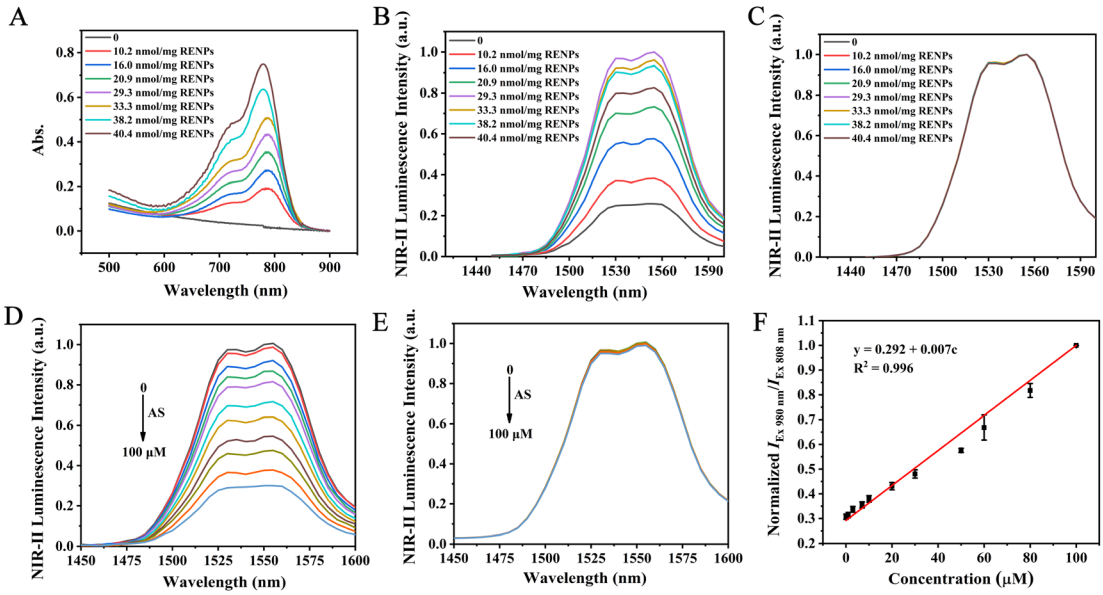

Fig. 3 (A) UV-vis absorption spectra of RENPs loaded with different amounts of Cy-TP. NIR-II luminescence spectra of RENPs after assembly with various amounts of Cy-TP under 808 nm (B) and 980 nm (C) laser excitation. NIR-II luminescence spectra of Cy-TP-RENPs after responding to different concentrations of HNO under 808 nm (D) and 980 nm (E) laser excitation. (F) A linear relationship between HNO concentration and the ratio value of $I_{Ex\ 980\ nm}/I_{Ex\ 808\ nm}$, which was calculated according to the value of the peak intensity at 1550 nm upon 980 and 808 nm excitations, respectively.

$_{980\ nm}/I_{Ex\ 808\ nm}$ increased with HNO in a concentration-dependent manner and showed a good linear relationship with [HNO] in the range of 0–100 μM ($R^2 = 0.994$, Fig. 3F). The linear equation was $I_{Ex\ 980\ nm}/I_{Ex\ 808\ nm} = 0.022c + 1.002$ (c is the concentration of HNO) and the limit of detection was 0.19 μM, which was calculated using the $3\sigma/k$ method (σ is the standard deviation of seven blank samples, and k is the slope of the linear fit in Fig. 3F). In addition, there was no obvious variation in the ratiometric signal of $I_{Ex\ 980\ nm}/I_{Ex\ 808\ nm}$ after incubation with other interfering substances, including metal ions, amino acids, ROS, RNS, and biothiols, demonstrating that Cy-TP-RENPs possessed a superior specificity for HNO (Fig. S12†). Moreover, Cy-TP-RENPs and the reaction product, Cy-HNO-RENPs, offered stable ratiometric signals within 48 h in various media, such as Tris–HCl buffer, FBS, and DMEM (Fig. S13A†). Incubation of Cy-TP-RENPs and Cy-HNO-RENPs in buffer solutions with different pH (pH = 4.0–8.0) caused a slight variation in the ratiometric signal (Fig. S13B†). In addition, the hydrodynamic diameter of Cy-TP-RENPs measured by dynamic light scattering remained unchanged within 7 days, indicating superior colloidal stability of Cy-TP-RENPs (Fig. S13C†). These results revealed that the as-prepared probe can rapidly respond to HNO with high specificity and that the probe and reaction products both present good stability in the physiological environment, providing a potential tool for detecting HNO *in vivo*.

Imaging HNO with Cy-TP-RENPs *in vivo*

Before imaging HNO *in vivo*, the biosafety of Cy-TP-RENPs was evaluated. First, the cytotoxicity of Cy-TP-RENPs was accessed by the CCK-8 method. As illustrated in Fig. S14,† the survival rate of HepG2 cells was >90% after incubation with different concentrations of Cy-TP-RENPs (0–0.6 mg mL^{-1}) for 24 h. The low cytotoxicity of Cy-TP-RENPs was also reflected by confocal fluorescence images of HepG2 cells co-stained with Calcein-AM and PI. As shown in Fig. S15,† after incubation with Cy-TP-RENPs for 24 h, the cells in each group still displayed strong green fluorescence from living cells and negligible red fluorescence from dead cells. Furthermore, different concentrations of Cy-TP-RENPs (0, 5, and 10 mg per 100 g body weight) were intravenously (i.v.) injected into healthy mice to investigate its biosafety at the living-body level. After 7 days, the blood biochemical and other routine parameters of the mice in experimental groups did not show an obvious difference from the control group (Fig. S16†). The hematoxylin and eosin (H&E) staining of major organs, including the heart, liver, spleen, lungs, and kidneys, showed no remarkable difference among the mice injected with or without Cy-TP-RENPs, illustrating that Cy-TP-RENPs caused no obvious damage to mice (Fig. S17†). All the above results demonstrated Cy-TP-RENPs to have good biocompatibility, guaranteeing their application for *in vivo* bioimaging.

We applied the probe to image HNO in living mice. As a start, we looked into the metabolic time of Cy-TP-RENPs in mice bodies. As shown in Fig. S18,† after injecting Cy-TP-RENPs into Balb/c mice, NIR-II luminescence signal was observed in the liver in 30 min, where it reached the maximum within 3 h, and then gradually decreased until 36 h, revealing that this nanoprobe can enrich in the liver and be metabolized there as well. Next, we utilized the nanoprobe to image exogenous HNO in the liver by intraperitoneal (i.p.) injection with AS 2 h after the injection of Cy-TP-RENPs. As shown in Fig. S19A and B,† the mice displayed a gradually attenuated NIR-II luminescence signal under 808 nm laser excitation ($I_{Ex\ 808\ nm}$) as the dosage of AS was elevated (0, 25, and 62.5 μg per 100 g of body weight). To confirm that this change in $I_{Ex\ 808\ nm}$ signal resulted from the external HNO, another group of mice was pretreated with glutathione (GSH) before injection of AS (62.5 μg per 100 g of body weight), which could deplete HNO, for NIR-II imaging. As expected, the $I_{Ex\ 808\ nm}$ signal was enhanced. Notably, the mice treated with GSH only (without AS) exhibited a higher $I_{Ex\ 808\ nm}$ signal than the control group, which can be ascribed to the reduction of endogenous HNO by GSH. During this process, NIR-II luminescence intensities excited by the 980 nm laser ($I_{Ex\ 980\ nm}$) in all groups only changed slightly (Fig. S19A and C†), thus being suitable for serving as the internal calibration signal of the ratiometric probe. By calculating the ratio values of $I_{Ex\ 980\ nm}/I_{Ex\ 808\ nm}$ in each group (Fig. S19D†), we can see that the ratiometric signals changed in an [HNO]-dependent manner, suggesting that the as-prepared nanoprobe could sensitively respond to HNO *in vivo*.

We also examined the capability of Cy-TP-RENPs to detect endogenous HNO during a drug-induced liver injury (DILI) process. Acetaminophen (APAP), a painkiller that can cause severe liver damage and is commonly used to construct DILI models,[23] was i.p. injected into mice. Two experimental groups of mice were injected with different dosages of APAP (10 and 20 mg per 100 g of body weight, group b and c), respectively, and the mice in the control group were given PBS only (group a). After APAP stimulation for 12 h, the mice in all groups were i.v. injected with Cy-TP-RENPs, followed by *in vivo* NIR-II luminescence imaging under 808 and 980 nm excitation after 3 h. As shown in Fig. S20A and B,† as compared with the control group, $I_{Ex\ 808\ nm}$ signals in groups b and c were significantly decreased with an increase in the dosage of APAP. Meanwhile, $I_{Ex\ 980\ nm}$ signals in groups b and c were slightly lower than that in the control group, indicating that the individual difference in mice, such as their metabolic capacity and tissue thickness, may lead to signal fluctuation (Fig. S20A and C†). To exclude these target-concentration-independent signal variations, the ratio values of $I_{Ex\ 980\ nm}/I_{Ex\ 808\ nm}$ in each group were calculated. The ratio values of experimental groups were 1.5 times (group b) and 2.3 times (group c) higher than that of the control group, respectively (Fig. S20A and D†), telling that the HNO level was increased and related to the degree of injury during DILI. In addition, we studied the intervention effect of α-lipoic acid (α-LA) on DILI, which was reported to effectively inhibit hepatotoxicity induced by APAP.[21] With the administration of α-LA (5 mg per 100 g of body weight, group d), $I_{Ex\ 808\ nm}$ signal was elevated and accordingly the $I_{Ex\ 980\ nm}/I_{Ex\ 808\ nm}$ ratio decreased significantly, indicating the down-regulation of [HNO] with the alleviation of DILI. These results suggested that Cy-TP-RENPs were able to successfully respond to endogenous HNO in a stimulator dosage-dependent manner.

Visualizing HNO in the HIRI process

Having verified the ability of Cy-TP-RENPs to report the change in HNO levels *in vivo*, we employed the nanoprobe to disclose the role of HNO in HIRI and monitor its progression. Since hepatic ischemia-reperfusion (HIR) contains two successive processes, *i.e.*, ischemia and reperfusion, we first applied the as-prepared nanoprobe to detect the HNO level in HIRI with different ischemic durations and a fixed reperfusion time of 24 h. HIRI models were established for mice according to previous reports,[24,25] in which the portal vein and hepatic artery were clamped with hemostatic clips for 0 (the sham group serving as the control), 30, 60, and 90 min ischemia, followed by reperfusion for 24 h after releasing the hemostatic clips (Fig. 4A). During the ischemia process, the liver showed pale color due to the blocked blood supply, while sanguineous perfusion was observed upon removal of the hemostatic clips. The Cy-TP-RENP nanoprobe was then i.v. injected into the mice, and NIR-II luminescence imaging was performed at different time points to observe the changes in the HNO levels. As shown in Fig. 4B, the liver area of the mice in the sham group exhibited gradually enhanced NIR-II luminescence signals upon excitation with both 808 nm and 980 nm laser within 180 min because of the gradual enrichment of probe in the liver. Meanwhile, the ratiometric signal in the liver was slightly increased due to the response of the probe to intrinsic HNO. After the IR process, the

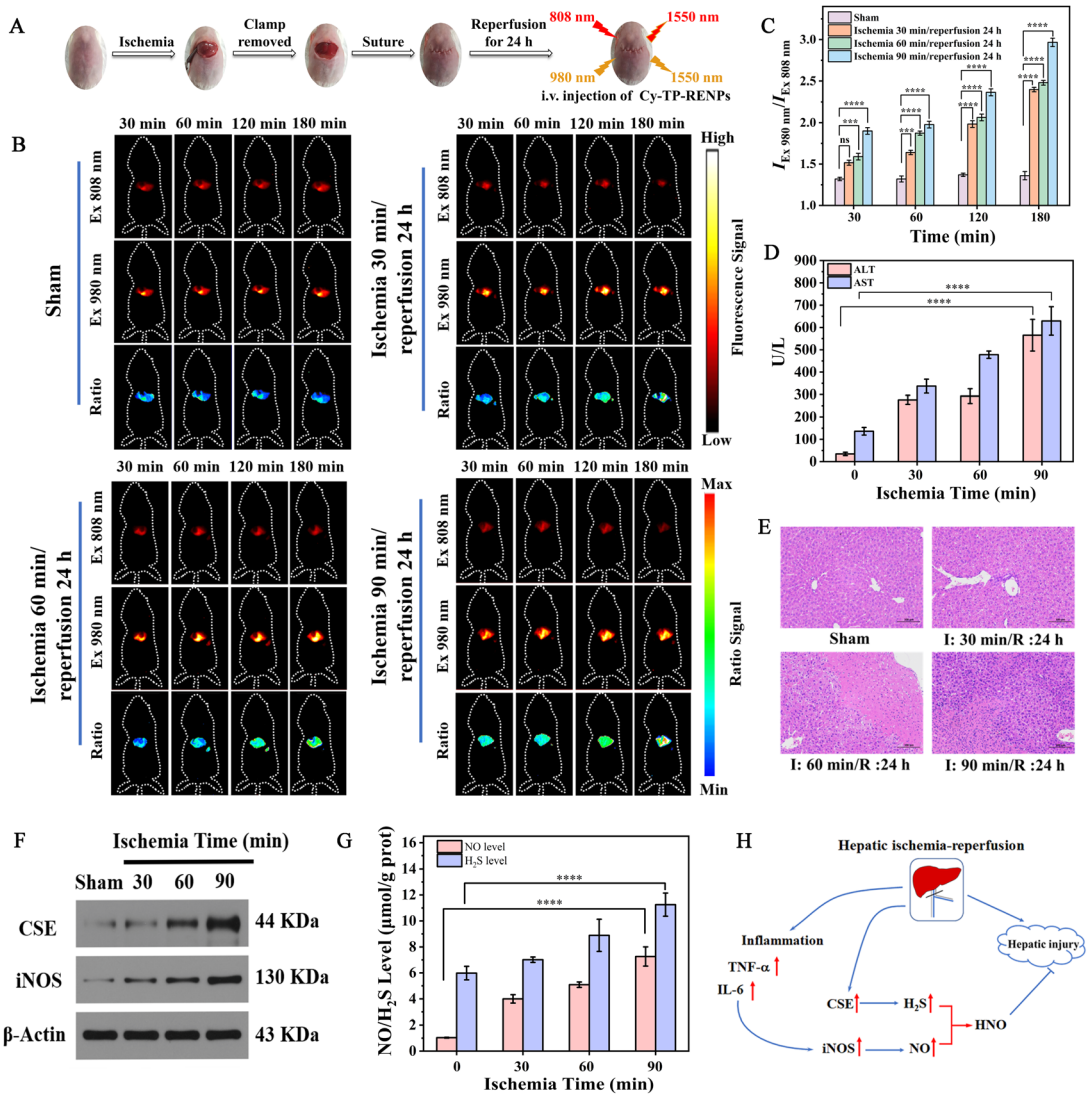

Fig. 4 (A) Photographs showing the surgery for the I/R process. (B) NIR-II luminescence imaging of mice with various treatments (sham-surgery group: ischemia for 0 min; I/R model: ischemia for 30 min, 60 min, or 90 min followed by reperfusion for 24 h) at different time points after i.v. injection of Cy-TP-RENPs and corresponding ratiometric imaging. (C) Ratio value ($I_{Ex\ 980\ nm}/I_{Ex\ 808\ nm}$) of the liver regions (B) at different time points. (D) Serum AST and ALT levels in the mice of various groups. (E) H&E staining of mice liver tissues from different groups (scale bar: 100 μm). (F) Expression levels of iNOS and CSE in mice livers of different groups detected by western blot. (G) The amounts of NO and H_2S in mice livers of different groups. All NIR-II images were obtained under 980 or 808 nm laser excitation with a 1300 nm long-pass filter. (H) Purposed biological synthesis route of HNO in mice liver with HIRI. Data are represented as the mean ± SD ($n = 5$), ***$P < 0.001$, ****$P < 0.0001$, ns: no statistically significant differences.

$I_{Ex\ 808\ nm}$ signal of the mice in ischemic groups was attenuated stepwise because of the overexpression of HNO. As compared with the sham group, the ratio values $I_{Ex\ 980\ nm}/I_{Ex\ 808\ nm}$ in the mice subjected to IR were remarkably enhanced up to 1.7, 1.8, and 2.2 times for ischemia with 30, 60, and 90 min at the observation time point of 180 min, respectively, demonstrating that higher amount of hepatic HNO was generated during IR process with longer ischemia time. Furthermore, the tendency of change in the ratio *versus* ischemia time was consistent at each observation time point, indicating Cy-TP-RENPs were stable enough for long-term visualization *in vivo* (Fig. 4C).

To evaluate the degree of liver injury during the IR process, we measured the enzyme activities of AST and ALT in serum, which were distinctly improved in ischemic groups with an ischemia time-dependent manner (Fig. 4D), confirming that the liver dysfunction was aggravated by prolonging the ischemia time in accordance with the previous reports.[26] Moreover, changes in pathological morphology in different groups were analyzed *via* H&E staining (Fig. 4E). Compared with the sham group, the cytoplasm was loose and lightly stained; meanwhile, hepatocyte necrosis and eosinophilia were increased in the IR group. And these conditions were more serious in the long-term ischemia group than in the short-term ischemia group, further verifying the degree of liver injury was closely related to the ischemia time. The above results illustrated that HNO was upregulated after 24 h reperfusion and its level was closely related to the degree of injury.

According to previous reports, HNO can be generated from the interaction of nitric oxide (NO) and hydrogen sulfide (H_2S) under physiological conditions.[27–29] Thus, to dig up the biological synthesis way for HNO in mice liver with HIRI, the related protein expression in liver tissues was analyzed. The typical proinflammatory cytokines, including tumor necrosis factor-α (TNF-α) and interleukin-6 (IL-6), were detected by ELISA, and the results showed that these cytokines were up-regulated along with the ischemia time, testifying the occurrence of inflammation during IR process (Fig. S21†). As a consequence, inducible nitric oxide synthase (iNOS) was overexpressed in the mice liver of the IR group (Fig. 4F). Moreover, western blot results revealed that cystathionine-γ-lyase (CSE) level was also higher in the mice liver after IR treatment (Fig. 4F). Therefore, the levels of NO and H_2S in the liver tissue of the mice in IR groups assayed by ELISA were higher than that of the sham group and increased with prolonging the ischemia time, thereby leading to the overexpression of HNO (Fig. 4G and H).

Subsequently, we attempted to monitor the change in HNO levels during the HIRI process with a fixed ischemia time followed by varying times of reperfusion. After 90 min ischemia, the mice underwent subsequent reperfusion with different times, *i.e.*, 3, 6, 12, and 20 h, respectively. All groups were injected with Cy-TP-RENPs and *in vivo* NIR-II luminescence imaging was performed 3 h later. As shown in Fig. 5A and B, with prolonging the reperfusion time, the ratio value of $I_{Ex\ 980\ nm}/I_{Ex\ 808\ nm}$ decreased first, reached the minimum at a reperfusion time of 6 h, and then increased, indicating the reperfusion process caused a decrease in HNO levels until reperfusion for 6 h and an increase in HNO thereafter. In the meantime, serum ALT and AST levels peaked at 6 hours of reperfusion, followed by a decrease (Fig. 5C). These results jointly demonstrated the injury was the most serious at 6 h post reperfusion, in line with a previous study on HIRI.[30] To further explore the reason for this HNO fluctuation, we analyzed the expression levels of iNOS and CSE protein at different time points during reperfusion. The expression level of CSE protein was firstly reduced until 6 h of reperfusion, which gradually increased; this was consistent with the change in the tendency of HNO. However, the iNOS expression was continuously up-regulated during reperfusion (Fig. 5D). Besides, as shown in Fig. 5E, the level of NO in the liver tissue gradually increased with an increase in reperfusion time, while the level of H_2S dropped to a minimum at 6 hours of reperfusion and then gradually increased. From these results, we speculated that CSE/H_2S system may be dominant in the biosynthesis of HNO under physiological conditions, leading to a similar variation tendency in the HNO content with that of H_2S. To perform a systematic and more comprehensive study, we also conducted two more sets of experiments where the ischemia time was separately fixed at 30 and 60 min, in which similar phenomena were also observed (Fig. S22 and S23†).

Revealing HNO as a product of stress reactions during HIRI

The above experimental results disclosed that the up-regulation of HNO was accompanied by the alleviation of HIRI after reperfusion for different durations, which implies that HNO may play an essential role in repairing HIRI and could potentially be a product of stress reaction. To confirm this hypothesis, we explored the influence of external HNO on HIRI, in which mice were pretreated with AS for 1 h before IR surgery. The mice were divided into four groups; among these, mice in the sham group (group a) keeping hepatic blood flow were used as the control, and mice in groups b–d were pretreated with different dosages of AS (b: 0 μg per 100 g of body weight, c: 50 μg per 100 g of body weight, d: 100 μg per 100 g of body weight) and then subjected to 90 min of ischemia and subsequent 24 h of reperfusion. At 3 h post-injection of Cy-TP-RENPs, *in vivo* NIR-II luminescence imaging was performed. Compared with the sham group, $I_{Ex\ 808\ nm}$ signals in groups b–d were significantly weakened with the increased dosage of AS (Fig. 6A). The ratio values of $I_{Ex\ 980\ nm}/I_{Ex\ 808\ nm}$ in each group were also calculated, which were enhanced with an [AS]-dependent manner (Fig. 6B), revealing HNO level was remarkably improved. Compared to mice subjected to HIR only (0 μg per 100 g of body weight of AS pretreated, group b), the concentrations of ALT and AST in the serum of groups c and d were decreased in an [AS]-dependent manner, revealing that pretreatment with AS significantly attenuated the liver dysfunction caused by IR injury (Fig. 6C). Furthermore, H&E staining further confirmed that there was no hepatocyte necrosis and inflammatory cell infiltration in the liver tissue of mice pre-treated with 100 μg per 100 g of body weight AS (Fig. S24†). These findings demonstrated that HNO can indeed protect hepatocytes against HIRI.

Subsequently, to investigate the protective mechanism of HNO, we looked into the HNO-induced discrepancy of gene

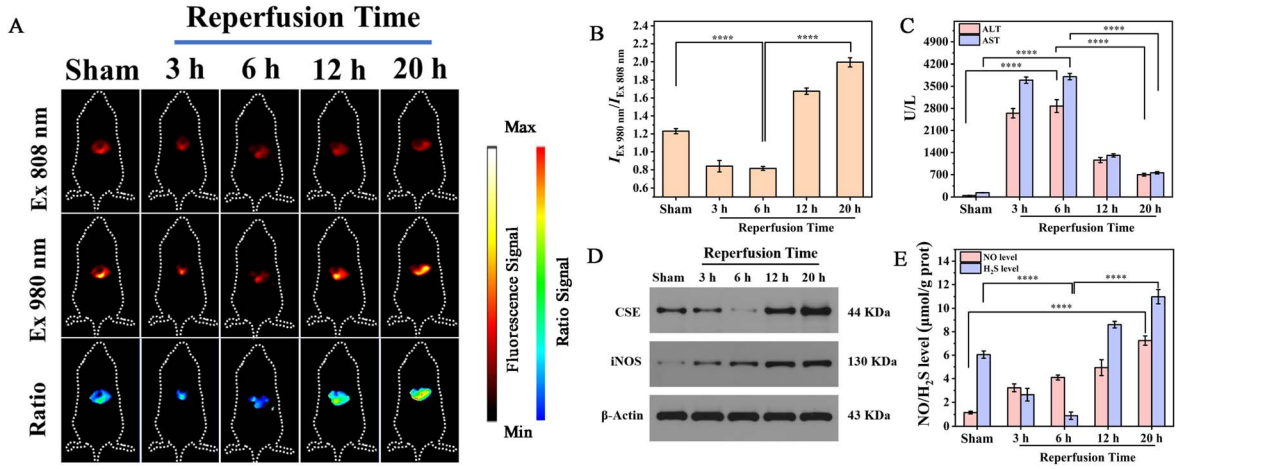

Fig. 5 (A) NIR-II luminescence imaging of the mice in the sham group (ischemia for 0 min) and I/R model group (ischemia for 90 min followed by reperfusion with different time) and corresponding ratiometric imaging. (B) Ratio value ($I_{Ex\ 980\ nm}/I_{Ex\ 808\ nm}$) of the liver regions in (A). (C) Serum ALT and AST levels in the mice of various groups. (D) Western blotting analysis of CSE and iNOS in mice liver from different groups. (E) The amounts of NO and H_2S in mice liver of different groups. All NIR-II images were obtained under 980 or 808 nm laser excitation with a 1300 nm long-pass filter. Data are represented as the mean ± SD ($n = 5$), ****$P < 0.0001$.

expression *in vivo*. RNA sequencing (RNA-seq) was conducted to compare the gene expression profiles of liver tissues from sham mice and IR model mice with or without HNO treatment. Fold change ≥2.0 and FDR <0.05 served as the screening conditions to screen out the differentially expressed genes (DEG) in each group. Hierarchical clustering analysis was employed to obtain the gene expression profile differences among the three groups. As shown in Fig. S25A,† clustering patterns of gene expression between the sham group and HNO-treated IR group were quite similar, while the clustering pattern from the IR model group was remarkably different, revealing the broad suppression of the pathologic state of liver tissue after pretreatment with HNO. A total of 3009 DEGs were identified from the IR group, relative to those from the sham group (Fig. 6D). Particularly, 1293 genes were up-regulated, while 1716 were down-regulated (Fig. S25B†). In addition, as compared with the IR group, a total of 2607 DEGs were identified in the HNO-IR group (Fig. 6D). Among them, 1515 and 1092 genes were up-regulated and down-regulated, respectively (Fig. S25C†). To gain a preliminary understanding of the potential function of these DEGs, we performed a functional analysis of markedly up-regulated and down-regulated genes. Gene ontology (GO) analysis showed that after pretreatment with HNO, up-regulated genes were mainly located in the biological processes of oxidation–reduction and liver-related metabolic processes (Fig. S26A†), while down-regulated genes were mainly enriched in apoptosis (Fig. S26C†). As for the IR group, IR injury-mediated up-regulated genes were primarily related to apoptosis, while down-regulated genes were associated with oxidation–reduction and liver-related metabolic processes (Fig. S26B and D†). According to the Kyoto Encyclopedia of Genes and Genomes (KEGG) pathway enrichment results, the down-regulated DEGs in the IR group, compared with the sham group, were mainly involved in retinol, steroid, Cyp450, and other metabolic pathways (Fig. S27A†). Moreover, the up-regulated DEGs were mainly related to MAPK, IL-17, FoxO, and p53 signaling pathways associated with inflammation and apoptosis (Fig. S27B†). Compared with the IR group, after HNO pretreatment, the up-regulated DEGs were mainly involved in retinol metabolism, cytochrome P450, and other metabolic processes, as well as the peroxisome pathway (Fig. 6E). On the contrary, the down-regulated DEGs were mainly involved in MAPK and IL-17 signaling pathways, which regulate inflammatory cytokines and apoptosis, respectively (Fig. 6F). Network analysis was further conducted by mapping genes from the top 20 (10 upregulated and 10 downregulated) most significantly HNO-affected pathways to the PPI network. The results showed that most of the top 10 hub genes in the up-regulated signaling pathways play a crucial role in metabolic processes, peroxisome, and Cyp450 pathways (Fig. 6G). Meanwhile, the most down-regulated hub genes, such as IL1β, Mapk7, HIF-1α, and Fos, exhibited a decisive effect on the inflammatory response and apoptosis (Fig. 6H). HNO promoted or repressed the expression of these hub genes *in vivo* (Fig. 6I and J), which further promoted the biological processes involved in metabolism and antioxidant action and inhibited the cascade signal transduction of inflammatory response. The above results revealed that the noteworthy alleviation of HIRI by HNO can be mainly attributed to the increase in pathological gene expression connected with metabolism and antioxidants, as well as the diminishment of pathological gene expression related to inflammatory activation.

To further verify the above results from the transcriptomic analysis, the secretion of proinflammatory factors and biomarkers of oxidative stress was investigated. Firstly, the content of TNF-α and IL-6 was measured to assess the inflammation response. As shown in Fig. S28A and B,† their expressions were remarkably elevated in the IR group than in the sham group and were significantly suppressed by the HNO pretreatment. This result revealed that HIRI induced an

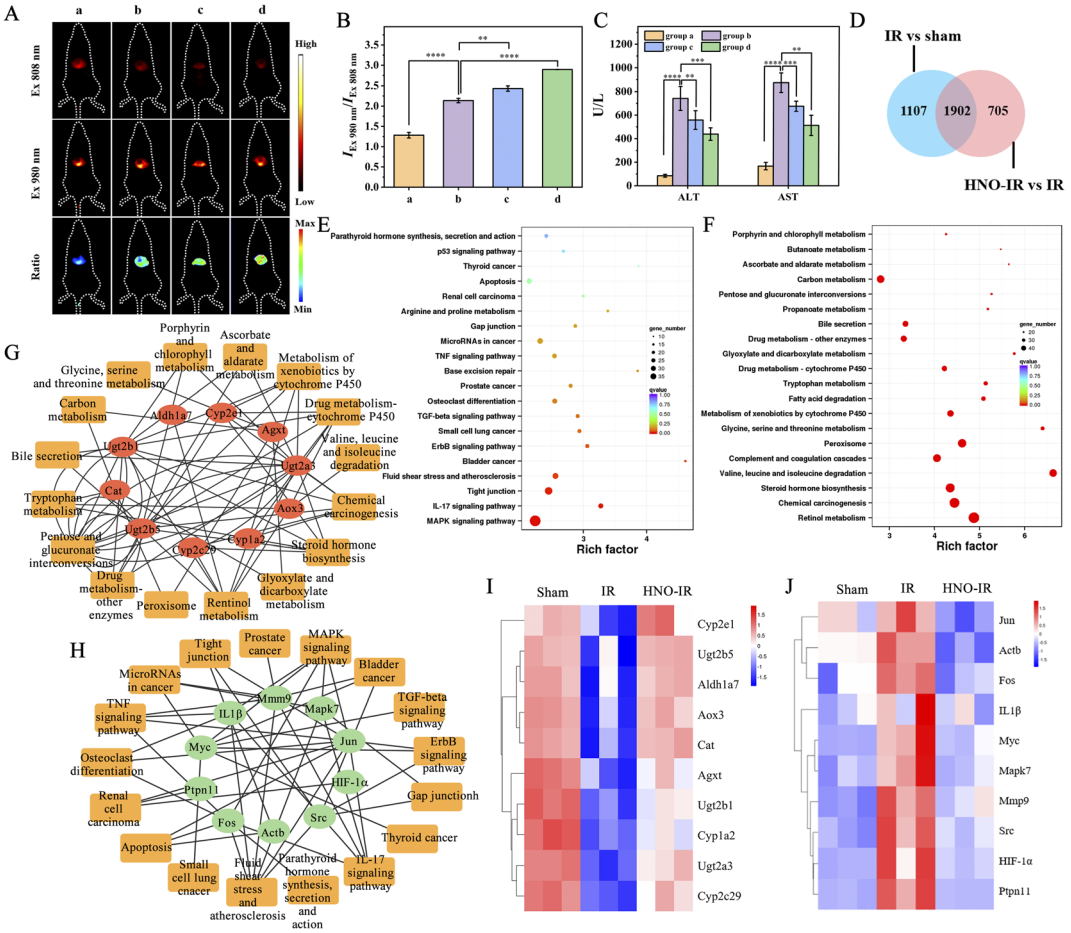

Fig. 6 (A) NIR-II luminescence imaging of the mice with different treatments (a: sham group: ischemia for 0 min; b: IR model mice with 90 min ischemia followed by 24 h reperfusion; c: IR model mice pretreated with 50 μg per 100 g of body weight of AS; d: IR model mice pretreated with 100 μg per 100 g of body weight of AS), and corresponding ratiometric imaging. (B) Ratio value ($I_{Ex\ 980\ nm}/I_{Ex\ 808\ nm}$) of the liver regions in (A). (C) Serum AST and ALT levels in the mice of various groups. (D) Venn diagram showing the overlap between the DEGs of the IR *vs.* sham group and the HNO-IR *vs.* IR group *in vivo*. KEGG pathways of up-regulated (E) and down-regulated (F) genes in the HNO-IR *vs.* IR group. Visualization of the up-regulated (G) and down-regulated (H) KEGG pathway top 10 hub genes. The gene network was constructed by mapping genes from the top 20 most significantly affected pathways to the PPI network. Heat map of top 10 up-regulated hub genes (I) and down-regulated hub genes (J). All NIR-II images were obtained under 980 or 808 nm laser excitation with a 1300 nm long-pass filter. Data are represented as the mean ± SD ($n = 5$), *$P < 0.05$, **$P < 0.01$, ***$P < 0.001$, ****$P < 0.0001$.

inflammatory response that could be relieved by external HNO. Besides, compared with the sham group, the IR group exhibited a higher level of malondialdehyde (MDA), lower enzyme activities of catalase (CAT), superoxide dismutase (SOD), and a lower level of GSH (antioxidant). This is explained by the ability of HIRI to decrease antioxidant enzyme activity and lead to the overproduction of ROS, which promotes lipid peroxidation to generate MDA as the end product. As expected, pretreatment with HNO significantly restrained hepatic oxidative stress in HIRI, improving the activity of CAT and SOD, as well as the GSH level, thus lessening the expression levels of MDA (Fig. S28C–F†). Furthermore, the variation tendency of the levels of these indicators displayed an HNO dosage-dependent manner. These results show that HNO can improve the anti-oxidative effect and inhibit oxidative damage, while relieving inflammation response and weakening the hepatocytes injury during the HIRI process, which is consistent with the transcriptomic analysis.

Conclusions

In conclusion, we developed an activatable ratiometric NIR-II nanoprobe based on RENPs for *in vivo* visualization of the fluctuation of HNO at the molecular level. Herein, the NIR-II luminescence of RENPs was regulated *via* the specific reaction between a small molecule and HNO. Taking advantage of NIR-II luminescence imaging, the probe featured deep tissue penetration, high spatial resolution, and contrast. The probe also exhibited excellent sensing performance toward HNO with high accuracy, sensitivity, and selectivity. The probe was successfully applied to track HNO levels during the HIRI process to reveal the relationship between HNO and HIRI, as well as the role of HNO as a product of stress reaction. We envision that our HNO-responsive NIR-II nanoprobe has the potential for application in disclosing the occurrence and progression of other HNO-involved events. We also anticipate that, after further studies,

HNO could be developed as an efficient protectant to alleviate hepatocyte injury during liver surgery.

Data availability

All the data associated with the research in this manuscript are available from the corresponding authors on reasonable request .

Author contributions

C. L., W. B., Z. L. (Zhen Li), and Z. L. (Zhihong Liu) conceived the project. C. L., W. B., and T. L. performed the experiments. C. L., Z. L. (Zhen Li), and Z. L. (Zhihong Liu) wrote the manuscript. All the other co-authors contributed to the data interpretation and revision of the manuscript.

Conflicts of interest

There are no conflicts to declare.

Acknowledgements

The work is supported by the National Natural Science Foundation of China (No. 22174035, 22004133) and the Hubei Province Outstanding Youth Foundation (2022CFA082). All experimental procedures were performed in accordance with institutional animal care guidelines. The Animal Ethics and Welfare Committee of Hubei University approved all procedures involving animal experiments.

Notes and references

1 W. A. Dar, E. Sullivan, J. S. Bynon, H. Eltzschig and C. Ju, *Liver Int.*, 2019, **39**, 788–801.
2 M. Cannistrà, M. Ruggiero, A. Zullo, G. Gallelli, S. Serafini, M. Maria, A. Naso, R. Grande, R. Serra and B. Nardo, *Int. J. Surg.*, 2016, **33**, S57–S70.
3 M.-Y. Wu, G.-T. Yiang, W.-T. Liao, A. P.-Y. Tsai, Y.-L. Cheng, P.-W. Cheng, C.-Y. Li and C.-J. Li, *Cell. Physiol. Biochem.*, 2018, **46**, 1650–1667.
4 D. N. Granger and P. R. Kvietys, *Redox Biol.*, 2015, **6**, 524–551.
5 D. Cheng, W. Xu, X. Gong, L. Yuan and X.-B. Zhang, *Acc. Chem. Res.*, 2021, **54**, 403–415.
6 S. Li, H. Li, X. Xu, P. E. Saw and L. Zhang, *Theranostics*, 2020, **10**, 1262–1280.
7 F. Doctorovich, P. J. Farmer and M. A. Marti, *The chemistry and biology of nitroxyl (HNO)*, Elsevier, Amsterdam, Netherlands 2016.
8 Y. Fang, J. Shang, D. Liu, W. Shi, X. Li and H. Ma, *J. Am. Chem. Soc.*, 2020, **142**, 15271–15275.
9 H. Yang, R. Li, Y. Zhang, M. Yu, Z. Wang, X. Liu, W. You, D. Tu, Z. Sun, R. Zhang, X. Chen and Q. Wang, *J. Am. Chem. Soc.*, 2021, **143**, 2601–2607.
10 S. Zhu, R. Tian, A. L. Antaris, X. Chen and H. Dai, *Adv. Mater.*, 2019, **31**, 1900321.
11 J. Li and K. Pu, *Chem. Soc. Rev.*, 2019, **48**, 38–71.
12 T.-B. Ren, Z.-Y. Wang, Z. Xiang, P. Lu, H.-H. Lai, L. Yuan, X.-B. Zhang and W. Tan, *Angew. Chem., Int. Ed.*, 2021, **60**, 800–805.
13 T. Wang, S. Wang, Z. Liu, Z. He, P. Yu, M. Zhao, H. Zhang, L. Lu, Z. Wang, Z. Wang, W. Zhang, Y. Fan, C. Sun, D. Zhao, W. Liu, J.-C. G. Bünzli and F. Zhang, *Nat. Mater.*, 2021, **20**, 1571–1578.
14 H. Wang, C. Liu, Z. He, P. Li, W. Zhang, W. Zhang and B. Tang, *Anal. Chem.*, 2021, **93**, 6551–6558.
15 J. Wang, W. Zhu, C. Li, P. Zhang, G. Jiang, G. Niu and B. Z. Tang, *Sci. China: Chem.*, 2020, **63**, 282–289.
16 R. Lv, M. Raab, Y. Wang, J. Tian, J. Lin and P. N. Prasad, *Coord. Chem. Rev.*, 2022, **460**, 214486.
17 T. Jia and G. Chen, *Coord. Chem. Rev.*, 2022, **471**, 214724.
18 J. Xu, A. Gulzar, P. Yang, H. Bi, D. Yang, S. Gai, F. He, J. Lin, B. Xing and D. Jin, *Coord. Chem. Rev.*, 2019, **381**, 104–134.
19 B. Zheng, J. Fan, B. Chen, X. Qin, J. Wang, F. Wang, R. Deng and X. Liu, *Chem. Rev.*, 2022, **122**, 5519–5603.
20 X. Song, S. Li, H. Guo, W. You, X. Shang, R. Li, D. Tu, W. Zheng, Z. Chen, H. Yang and X. Chen, *Angew. Chem., Int. Ed.*, 2019, **58**, 18981–18986.
21 T. Liang, Z. Li, P. Wang, F. Zhao, J. Liu and Z. Liu, *J. Am. Chem. Soc.*, 2018, **140**, 14696–14703.
22 T. Liang, Q. Wang, Z. Li, P. Wang, J. Wu, M. Zuo and Z. Liu, *Adv. Funct. Mater.*, 2020, **30**, 1910765.
23 M. R. McGill and H. Jaeschke, *BBA, Mol. Basis Dis.*, 2019, **1865**, 1031–1039.
24 W. Zhang, J. Liu, P. Li, X. Wang, S. Bi, J. Zhang, W. Zhang, H. Wang and B. Tang, *Biomaterials*, 2019, **225**, 119499.
25 X. Han, R. Wang, X. Song, F. Yu, C. Lv and L. Chen, *Biomaterials*, 2018, **156**, 134–146.
26 J. Chen, L. Chen, Y. Wu, Y. Fang, F. Zeng, S. Wu and Y. Zhao, *Nat. Commun.*, 2021, **12**, 1–15.
27 Y. Zhou, Z. Wu, X. Cao, L. Ding, Z. Wen and J.-S. Bian, *Pharmacol. Res.*, 2016, **111**, 885–895.
28 M. Eberhardt, M. Dux, B. Namer, J. Miljkovic, N. Cordasic, C. Will, T. I. Kichko, J. de la Roche, M. Fischer, S. A. Suárez, D. Bikiel, K. Dorsch, A. Leffler, A. Babes, A. Lampert, J. K. Lennerz, J. Jacobi, M. A. Marti, F. Doctorovich, E. D. Högestätt, P. M. Zygmunt, I. Ivanovic-Burmazovic, K. Messlinger, P. Reeh and M. R. Filipovic, *Nat. Commun.*, 2014, **5**, 1–8.
29 S. A. Suarez, P. Vargas and F. A. Doctorovich, *J. Inorg. Biochem.*, 2021, **216**, 111333.
30 M. Yang, Q. Du, J. Goswami, P. R. Varley, B. Chen, R.-H. Wang, A. E. Morelli, D. B. Stolz, T. R. Billiar, J. Li and D. A. Geller, *Hepatology*, 2018, **67**, 1056–1070.